

Ab initio Investigation of Magnetic Transport Properties by Wannier Interpolation

Yi Liu, Hai-Jun Zhang, and Yugui Yao*

*Institute of Physics and Beijing National Laboratory for Condensed Matter Physics,
Chinese Academy of Sciences, P. O. Box 603, Beijing 100190, China*

We present an efficient *ab initio* approach for the study of magnetic transport properties based on the Boltzmann equation with the Wannier interpolation scheme. Within the relaxation time approximation, band-resolved electric conductivity under a finite magnetic field is obtained and the historical motion of the electron wave packet in reciprocal space is determined. As a typical application of this method, we have calculated the electric conductivities of MgB₂ under finite magnetic fields. Multiband characters for the individual bands are revealed, and the field dependence of the conductivity tensor is studied systematically with the field orientated parallel and normal to the *c*-axis, respectively. The obtained historical motion is employed to simulate directly the cyclotron motion in the extremal orbit and determine the corresponding effective mass. Moreover, This approach is further exploited to calculate the Hall coefficient in the low-field limit, without the complicated computation for the second \mathbf{k} derivative of the band.

PACS numbers: 71.15.Dx, 71.18.+y, 75.47.-m

I. INTRODUCTION

Magnetic transport properties, such as magnetoresistance (magnetoconductivity) and the Hall effect, which have been investigated experimentally and theoretically for a long history, are of great importance in the field of research for metals and semiconductors. These properties are sensitively dependent on the topology of the Fermi surface (FS). The corresponding semiclassical interpretations were first given by Lifshitz *et al.*¹ in the light of the Boltzmann equation with a general collision operator. Subsequently they were further developed for the studies of magnetoresistance^{2,3} and Hall effect,⁴ respectively.

The Boltzmann transport theory has functioned successfully in previous studies for two-dimensional systems through analytical and numerical solutions.^{5–8} Yet in real three-dimensional crystals, transport behaviors are significantly determined by the complex FS, where models are not much satisfactory and analytical solutions are formidable. *Ab initio* study is then essential to provide the most comprehensive and reliable investigation. To our knowledge of magnetoresistance, so far works based on electronic structure calculation have been rarely concerned with the numerical solution of the Boltzmann equation for the band-resolved electric conductivity under the finite magnetic field.^{9,10} They were faced with either heavy *ab initio* computation of properties on the accurate FS, or unreliable results from the Shankland-Koelling-Wood (SKW) interpolation scheme^{11,12} in the presence of band crossings close to the FS. On the other hand, in the low-field limit the solution of the Boltzmann equation has been extensively studied for the Hall effect through the power-series expansion of the magnetic field.¹³ With the isotropic relaxation time approximation, the Hall coefficient is explicitly formulated for metals having cubic symmetry.⁴ Following this perturbation method, previous simulations were carried out based on empirical tight-binding (TB) band structures,¹⁴ *ab initio*

calculation combined with the SKW,¹⁵ and the Wannier interpolation scheme.¹⁶ However, only cubic metals were involved in these studies, and the second \mathbf{k} derivative of the band was necessary.

In this paper, we present an *ab initio* approach combined with the Wannier interpolation scheme for the solution of the Boltzmann equation within the relaxation time approximation. Band structures are obtained through the *ab initio* calculation, and Wannier functions (WFs) are then constructed.¹⁷ The Runge-Kutta scheme is employed to determine the historical motion of the electron wave packet, where the WFs are used to evaluate the local velocities. The numerical integration with the tetrahedron scheme¹⁸ is adopted to deal with the sum over \mathbf{k} -space. It is noticeable that the velocity evaluation with the aid of the Wannier interpolation is more efficient (reliable) than that using *ab initio* calculation (the SKW interpolation¹⁶) at individual \mathbf{k} points. We have already applied this magnetoconductivity simulation to the superconductor MgB₂¹⁹ in our previous Letter⁹ and the combination with the experimental measurements played a key role in deriving electron-phonon scattering times. In this work, we further study systematically the band-resolved electric conductivity of MgB₂ based on this approach, with the finite magnetic field orientated parallel and normal to the *c*-axis, respectively. The historical tracks obtained during the Runge-Kutta integration is also used to study directly the cyclotron motion of the electron wave packet in the extremal orbit. This provides a direct approach to determine the effective mass of the corresponding extremal orbit. Moreover, we are able to calculate the Hall coefficient in the low-field limit based on the conductivity simulation, which is applicable for crystals of arbitrary structures. Unlike the perturbation method, the complicated computation of the second \mathbf{k} derivative of the band is avoided.

The paper is organized as follows. The simulation method is presented in Sec. II. It is employed to study systematically the magnetoconductivity of MgB₂ in the

next section, where the simulation of the cyclotron motion of the electron wave packet is included. In Sec. IV, we calculate the low-field Hall coefficients for several cubic metals and hcp Mg. Conclusions are drawn in section V.

II. SIMULATION METHOD

With the powerful Wannier interpolation scheme,^{16,20} we calculate the band-resolved electric conductivity under a finite magnetic field through numerically solving the Boltzmann equation. In this section, all the ingredients involved in our simulation are detailed below.

A. Band-resolved electric conductivity

According to the Boltzmann transport theory within the relaxation time approximation, the dc electric conductivity tensor of a metal under a uniform magnetic field is written as²¹

$$\sigma^{(n)} = \frac{e^2}{4\pi^3} \int d\mathbf{k} \tau_n(\varepsilon_n(\mathbf{k})) \mathbf{v}_n(\mathbf{k}) \bar{\mathbf{v}}_n(\mathbf{k}) \left(-\frac{\partial f}{\partial \varepsilon}\right)_{\varepsilon=\varepsilon_n(\mathbf{k})}, \quad (1)$$

where n is the band index, $\tau_n(\varepsilon_n(\mathbf{k}))$ is the scattering time of the n -th band and assumed to be dependent on the wave vector \mathbf{k} only through the eigenvalue $\varepsilon_n(\mathbf{k})$. f is the Fermi-Dirac distribution. $\mathbf{v}_n(\mathbf{k})$ is the velocity given by the equation of motion

$$\mathbf{v}_n(\mathbf{k}) = \frac{1}{\hbar} \frac{\partial \varepsilon_n(\mathbf{k})}{\partial \mathbf{k}}. \quad (2)$$

$\bar{\mathbf{v}}_n(\mathbf{k})$ is a weighted average of the velocity over the past history of the electron passing through \mathbf{k} :

$$\bar{\mathbf{v}}_n(\mathbf{k}) = \int_{-\infty}^0 \frac{dt}{\tau_n(\mathbf{k})} e^{t/\tau_n(\mathbf{k})} \mathbf{v}_n(\mathbf{k}_n(t)). \quad (3)$$

The magnetic field is explicitly acting on the time evolution of $\mathbf{k}_n(t)$, as given in the equation of motion:

$$\frac{d\mathbf{k}_n(t)}{dt} = -\frac{e}{\hbar} \mathbf{v}_n(\mathbf{k}_n(t)) \times \mathbf{B}, \quad (4)$$

with the initial condition $\mathbf{k}_n(0) = \mathbf{k}$. We start with this condition for one \mathbf{k} point and simulate reversely the time evolution given by Eq. (4). It is physically reasonable and mathematically maneuverable, and follows a typical Runge-Kutta method to deal with the equations of motion. The velocity at an arbitrary \mathbf{k} points is evaluated analytically through the Wannier interpolation,¹⁶ as detailed in the following subsections. A serial of $\mathbf{k}(t)$ points is obtained as a result of the Runge-Kutta integration for each initial \mathbf{k} point. They sample the history track of the electron wave packet at the corresponding time. Consequently, $\bar{\mathbf{v}}(\mathbf{k})$, according to Eq. (3), can be obtained as

the weighted average of the velocities at these $\mathbf{k}(t)$ points along the track. Then the integration in Eq. (1) is performed by employing the modified tetrahedron scheme.¹⁸

As in most cases, the relaxation time for each band is not easily determined. Therefore, we incorporate the magnetic field B and the relaxation time τ as one variable $B\tau$, which relates to an important dimensionless quantity $\omega\tau = \frac{e}{m^*} B\tau$, with m^* the effective mass. Phenomenally, $\omega\tau$ represents the completed part in the cyclotron orbit before the carrier is scattered out.

An implicit rule holds in the semiclassical framework: the magnetic field does not affect the kinetic energy of the carrier. Thus it imposes a severe restriction on every point in the $\mathbf{k}(t)$ serials that they are all sampled from the same constant-energy surface. It is a straightforward consequence from the theoretical viewpoint, but not accomplished automatically in the numerical simulation. In our code, we developed a modified self-adaptive Runge-Kutta scheme, which takes much less time than the regular Runge-Kutta methods to achieve the same accuracy. We did convincing tests for several arbitrary initial \mathbf{k} points and found that the energies in their $\mathbf{k}(t)$ serials were converged better than 10^{-7} Hartree.

B. Wannier interpolation

In our simulation, the velocity at an arbitrary \mathbf{k} point is evaluated through analytical calculation with the Wannier interpolation scheme. WFs are constructed as a “postprocessing” operation based on Bloch eigenstates and eigenvalues obtained through a standard *ab initio* electronic structure calculation carried out on a uniform k -point grid.¹⁷ Here we employ the ultrasoft-pseudopotential²² plane-wave method with generalized-gradient approximation²³ for the exchange and correlation potential. We give a brief review about the Wannier interpolation as follows, while details can be found in Ref. 17. We use the symbol \mathbf{q} to denote the points on the *ab initio* mesh, and \mathbf{k} for arbitrary and interpolation-grid points.

The eigenstate $|\psi_{n\mathbf{q}}\rangle$ is obtained after the electronic structure calculation. Its periodic part is defined as $u_{n\mathbf{q}}(\mathbf{r}) = e^{-i\mathbf{q}\cdot\mathbf{r}} \psi_{n\mathbf{q}}(\mathbf{r})$. Denoting the Wannier function in the cell \mathbf{R} within the band n as $|\mathbf{R}n\rangle$, we have

$$|\mathbf{R}n\rangle = \frac{V}{(2\pi)^3} \int d\mathbf{q} e^{-i\mathbf{q}\cdot\mathbf{R}} |\psi_{n\mathbf{q}}\rangle, \quad (5a)$$

$$|\psi_{n\mathbf{q}}\rangle = \sum_{\mathbf{R}} e^{i\mathbf{q}\cdot\mathbf{R}} |\mathbf{R}n\rangle. \quad (5b)$$

Here V is the volume of the real-space primitive cell. As shown in Eq. (5a), the freedom in the choice of the phases of the Bloch states results in the arbitrariness of the Wannier functions. By minimizing their total delocalization with respect to the phase freedom, the unique set of maximally localized Wannier functions is determined. The corresponding Bloch-like functions $|u_{n\mathbf{q}}^{(W)}\rangle$ are then

obtained according to Eq. (5b). The superscript (W) or (H) marks the quantities belonging to the Wannier or Hamiltonian gauge, respectively.^{16,20} Straightforwardly we obtain the Hamiltonian by

$$H_{nm}^{(W)}(\mathbf{q}) = \langle u_{n\mathbf{q}}^{(W)} | \hat{H}(\mathbf{q}) | u_{m\mathbf{q}}^{(W)} \rangle. \quad (6)$$

With a Fourier transform, we have

$$\langle \mathbf{0}n | \hat{H} | \mathbf{R}m \rangle = \frac{1}{N_q^3} \sum_{\mathbf{q}} e^{-i\mathbf{q}\cdot\mathbf{R}} H_{nm}^{(W)}(\mathbf{q}), \quad (7)$$

where \hat{H} is the effective one-particle Hamiltonian. The sum runs over all the \mathbf{q} points on the *ab initio* mesh. Finally the interpolation is implemented by transforming back the matrix $\langle \mathbf{0}n | \hat{H} | \mathbf{R}m \rangle$ to an arbitrary \mathbf{k} point,

$$H_{nm}^{(W)}(\mathbf{k}) = \sum_{\mathbf{R}} e^{i\mathbf{k}\cdot\mathbf{R}} \langle \mathbf{0}n | \hat{H} | \mathbf{R}m \rangle. \quad (8)$$

The Hamiltonian at any \mathbf{k} point is then analytically determined.

C. Evaluation of velocity

To calculate the velocity, we diagonalize the above interpolated Hamiltonian by finding a unitary rotation matrix $U(\mathbf{k})$:

$$H^{(H)}(\mathbf{k}) = U^\dagger(\mathbf{k}) H^{(W)}(\mathbf{k}) U(\mathbf{k}), \quad (9)$$

where $H_{nm}^{(H)}(\mathbf{k}) = \varepsilon_{n\mathbf{k}}^{(H)} \delta_{nm}$, and $\varepsilon_{n\mathbf{k}}^{(H)}$ are identical to the eigenvalues obtained from the *ab initio* calculation at $\mathbf{k} = \mathbf{q}$. We then evaluate the velocities for an arbitrary \mathbf{k} point through

$$\mathbf{v}_n(\mathbf{k}) = \frac{1}{\hbar} \frac{\partial \varepsilon_n^{(H)}(\mathbf{k})}{\partial \mathbf{k}} = \frac{1}{\hbar} \frac{\partial}{\partial \mathbf{k}} H_{nn}^{(H)}. \quad (10)$$

Note that the WFs are constructed via discrete Fourier transform based on the *ab initio* band structure. The interpolation will not be jeopardized by band crossings and avoided crossings.^{16,20}

III. MAGNETOCONDUCTIVITY UNDER FINITE MAGNETIC FIELDS

As the first remarkable application of our approach, we study the electric conductivities of normal-state MgB₂ under finite magnetic fields. This superconductor has been investigated extensively in recent years.^{26–29} In our previous Letter⁹, the simulation method presented in Sec. II was employed and the combination with the experimental measurements provided a unique way to obtain band-resolved scattering rates in multiband systems. In this work, we further study thoroughly the anisotropic magnetoconductivity of MgB₂ with the magnetic field orientated parallel and normal to the *c*-axis, respectively.

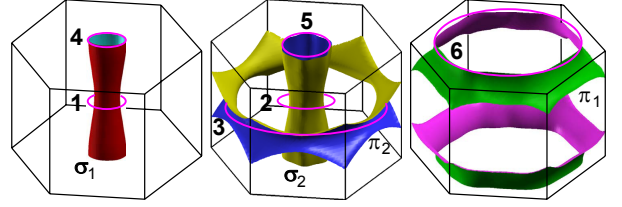


FIG. 1: (color online) The calculated Fermi surface of MgB₂ and the extremal orbits labelled for the magnetic field along the *c*-axis.

TABLE I: The asymptotic behaviors of the diagonal elements of the electric conductivity tensor of MgB₂ in the classical high-field limit. The coordinate system is defined with the *c*-axis along the *z* direction.

Field	Band	Orbit	σ_{xx}	σ_{yy}	σ_{zz}
$\mathbf{B} \parallel \hat{z}$	σ_1, σ_2	Closed	$\sim B^{-2}$	$\sim B^{-2}$	$\sim B^0$
	π_1, π_2	Closed	$\sim B^{-2}$	$\sim B^{-2}$	$\sim B^0$
$\mathbf{B} \parallel \hat{x}$	σ_1, σ_2	Open	$\sim B^0$	$\sim B^0$	$\sim B^{-2}$
	π_1, π_2	Closed	$\sim B^0$	$\sim B^{-2}$	$\sim B^{-2}$

The FS of MgB₂ consists of four sheets. Two forming slightly warped cylinders come from a couple of “hole-like” quasi-two-dimensional bands (bonding σ_1 and antibonding σ_2), and two tubular sheets form the three-dimensional π bands (antibonding π_1 and bonding π_2), as shown in Fig. 1. With the magnetic field along the *c*-axis, there are six extremal orbits centered around Γ and A , as labelled in Fig. 1 by numbers 1-3 and 4-6, respectively. The coordinate system is set with the *c*-axis along the *z* direction throughout the conductivity calculation.

Before calculating the magnetoconductivity of MgB₂, we first analyze its asymptotic behavior for each band in the classical high-field limit. According to the Boltzmann transport theory, the change in electric conductivity under a finite magnetic field arises from the cyclotron motion of the electron driven by the field. In general, contributions from the cyclotron motions in a closed orbit and an open orbit have different field dependences. Following the analytical deduction by Lifshitz *et al.*¹, and the qualitative analysis by Pippard²⁴ and Fawcett²⁵ based on the geometric features of the FS, we can determine the asymptotic behavior of the diagonal element of the electric conductivity tensor of MgB₂, as summarized in Table 1. It is helpful to check the validity of the following numerical simulation under finite magnetic fields.

A. Magnetic field along the *c*-axis

When the field is applied in the *c* direction, all the four Fermi sheets are composed of closed orbits. We use Eq. (1) to calculate the electric conductivity along the *x*-axis in the *ab* plane. σ_{xx}/τ of the four bands are shown

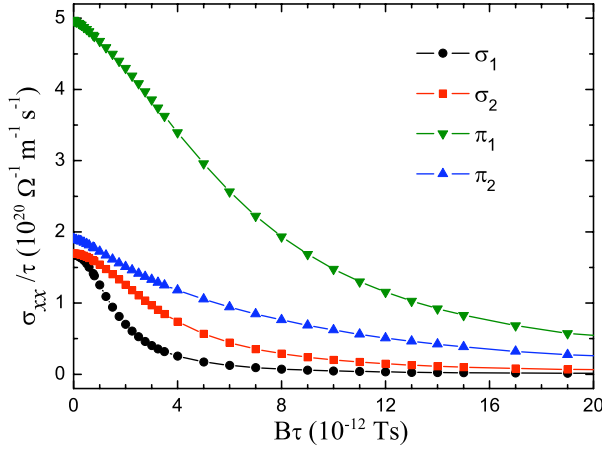


FIG. 2: (color online) σ_{xx}/τ as a function of $B\tau$ of the four bands of MgB₂, with the magnetic field along the *c*-axis.

in Fig. 2.

The simulation is carried out with the FS refined after the conventional electronic structure calculation.¹⁸ With the magnetic field along the 6-fold rotation axis, the symmetry of the system are reduced by half, and σ_{yy} , which are not plotted here, behave the same as σ_{xx} .³⁰ The field dependence of the band-resolved σ_{xx} can be described well with a dominant term B^{-2} ,⁹ in good agreement with the asymptotic behavior in Table 1. Since the magnitudes of σ_{xx}/τ of the two π bands in Fig. 2 are noticeably different, understanding of generalized σ and π bands might be incomplete, and the individual bands deserve further studies.

As stressed in Sec. II, the historical motion of the electron wave packet in reciprocal space is obtained in the process of the conductivity calculation. We take advantage of these cyclotron motions in the extremal orbits of the four bands to determine the corresponding effective masses. It provides a straightforward approach to investigate the extremal orbit and effective mass, which is usually a major concern of the study of the de Hass-van Alphen (dHvA) effect.^{31–33}

In one of these previous studies of the dHvA effect in MgB₂, the calculation was carried out with $m^* = \frac{\hbar}{2\pi} \oint \frac{d\mathbf{k}}{|\nabla(\mathbf{k})|}$, and provided the absolute values of the effective masses.³¹ Later, Mazin *et al.*³³ obtained the effective mass through the standard formula: $m^* = \frac{\hbar^2}{2\pi} (\frac{\partial \mathcal{A}}{\partial E})_{k_z}$, with \mathcal{A} the area of the orbit, which was computed in small energy ranges around the Fermi level.

In our case, the cyclotron motion of the electron wave packet at the FS is tracked accurately with the serial of $\mathbf{k}(t)$ points obtained through the self-adaptive Runge-Kutta integration for every initial \mathbf{k} point. Particularly, in the extremal orbits, as labelled in Fig. 1, we choose one initial \mathbf{k} point each to study the historical motion. As an example, we plot in Fig. 3 two of these historical tracks in Orbit 1 and Orbit 3, respectively.

These sinusoidal-like curves shown in Fig. 3 illustrate

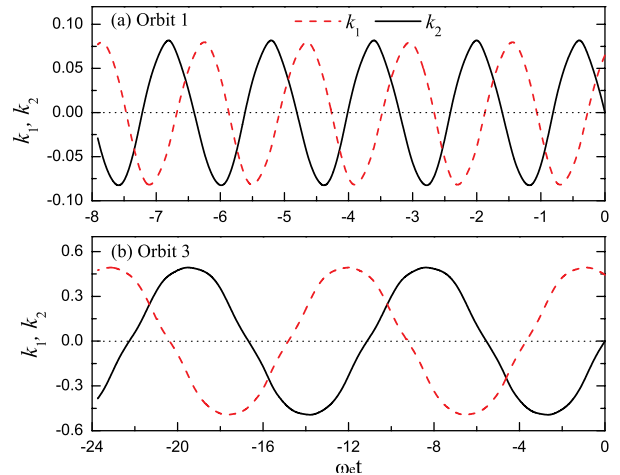


FIG. 3: (color online) Historical track of the electron wave packet in reciprocal space. The initial positions are $\mathbf{k}(0.065, 0.0, 0.0)$ in Orbit 1 (a), and $\mathbf{k}(0.444, 0.0, 0.0)$ in Orbit 3 (b), respectively. \mathbf{k} points are expressed as $\mathbf{k}(k_1, k_2, k_3)$, in the unit of reciprocal lattice vectors. There are 4000 points on each curve. k_3 is fixed in the Γ plane during the simulation. The abscissa $\omega_e t$ is related to Bt as $\omega_e t = \frac{e}{m_e} Bt$, where m_e is the mass of a free electron.

TABLE II: Calculated effective masses in the extremal orbits of MgB₂, given in the unit of the free-electron mass.

Orbit:	1	2	3	4	5	6
Ref. 31	0.254	0.313	1.699	0.550	0.612	0.924
Ref. 33	-0.251	-0.543	1.96	-0.312	-0.618	-1.00
This work	-0.255	-0.541	1.816	-0.309	-0.656	-0.988

vividly the cyclotron motion in reciprocal space driven by the magnetic field. The period of the motion, \mathcal{T} , can be read directly from the figure. The effective mass of the corresponding extremal orbit is then straightforwardly obtained in the absolute value as $|m^*|/m_e = \mathcal{T}/2\pi$, where m_e is the free-electron mass. Then the sign of the effective mass is determined through analyzing the direction of the cyclotron motion. As shown in Fig. 3, the cyclotron motion in Orbit 3 is anticlockwise, while it is clockwise in Orbit 1, as well as those in the rest four extremal orbits. It is then concluded that the third orbit is “electronlike”, while the rest of all are “holelike”. Our results, listed in Table 2, show good agreement with the previous studies, which confirms the validity of the approach.

In the rest of this subsection, we return to the investigation of band-resolved electric conductivity. In the current geometry, the Hall conductivity, σ_{xy} , is another non-trivial element besides σ_{xx} . In our previous Letter,⁹ the Hall conductivity was calculated with Eq. (1) for all the four bands. A sign change from positive to negative has been found in the π_2 band with increasing field, while the π_1 and the two σ bands behave simply as holes. For a

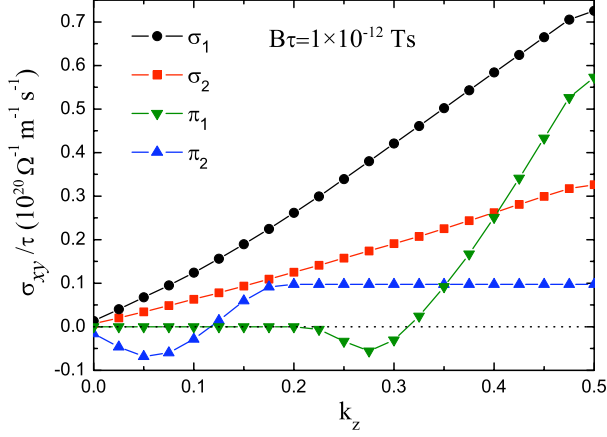


FIG. 4: (color online) The partial Hall conductivity $\sigma_{xy}^{(n)}(k_z)/\tau^{(n)}$ contributed by orbits between $-k_z$ to k_z of the individual bands as a function of k_z .

thorough understanding, we further perform the partial integration for the Hall conductivity, $\sigma_{xy}^{(n)}(k_z)/\tau^{(n)}$, by

$$\begin{aligned} \sigma_{xy}^{(n)}(k_z)/\tau^{(n)} &= \frac{e^2}{4\pi^3} \int dk_x dk_y \int_{-k_z}^{k_z} dk_z v_x^{(n)}(\mathbf{k}) \bar{v}_y^{(n)}(\mathbf{k}) \\ &\times \left(-\frac{\partial f}{\partial \varepsilon}\right)_{\varepsilon=\varepsilon_n(\mathbf{k})}. \end{aligned} \quad (11)$$

We employ a $30 \times 30 \times 40$ mesh, which gives 3192 \mathbf{k} points in the irreducible Brillouin zone. The extra finer grid along the z -axis is adopted for the integration from $-k_z$ to k_z . $B\tau$ is fixed at 1.0×10^{-12} Ts.

The calculated partial Hall conductivity of the four bands is shown in Fig. 4. For the two σ bands, the linear growth is understood with the cylindrical shape of the Fermi sheets. For the two π bands, there are sign changes along the k_z axis, which confirm that multiband character exists in the individual π bands. Although the π_1 band was considered “electronlike” according to the band structure, “holelike” part occupies most of the Fermi sheet except for the small peaks close to the Γ plane. Thus it behaves as a hole in the full Hall conductivity with the increasing magnetic field.⁹ Yet while the situation is opposite for the π_2 band. The small hills are “holelike”, and the big belly is “electronlike”. Thanks to the *ab initio* simulation of band-resolved conductivity, we have obtained such detailed knowledge of the multiband character for the individual bands in MgB₂.

B. Magnetic field normal to *c*-axis

When the magnetic field is normal to *c*-axis, different transport behaviors are expected due to the hexagonal structure of MgB₂. We further study this geometry by applying the field along the *x*-axis in the *ab* plane. The one-dimensional infinity of the two σ bands is then exposed, and the tubular π bands consist of closed orbits in

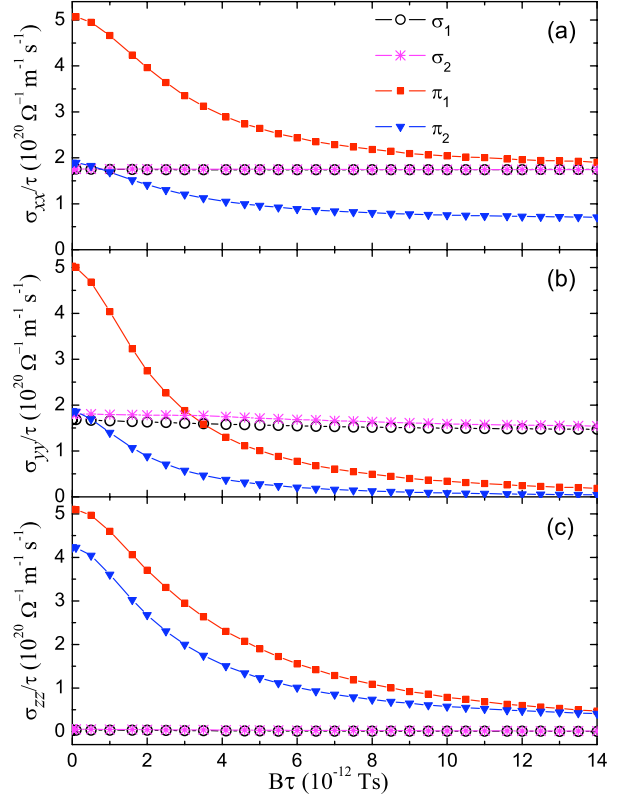


FIG. 5: (color online) $B\tau$ dependences of σ_{xx}/τ (a), σ_{yy}/τ (b), and σ_{zz}/τ (c) of the four bands of MgB₂. The magnetic field is applied along the *x*-axis in the *ab* plane.

the planes normal to the field, including extended closed orbits.

We calculate the electric conductivity tensor using Eq. (1). Symmetry is further reduced because the 6-fold rotation axis has vanished in the current geometry. The three diagonal elements of the conductivity tensor are shown in Fig. 5.

There are two categories of field-dependent behaviors of the diagonal elements. For the two σ bands, conductivity elements show little dependence on the magnetic field. In the *x* direction, the motion of the electron wave packet is not affected by the field, rendering σ_{xx} field-independent. Similar behavior in the *y* direction is accounted for by open orbits in the two (nearly standard) cylinders.^{1,24} The *z*-components of Fermi velocities are negligible compared to those in the other two directions. This provides an elegant interpretation for the almost vanished elements σ_{zz} . The two π bands are composed of closed orbits with the magnetic field along the *x*-axis. As the field increases, σ_{xx} of the two π bands decrease and tend to saturation in the high-field limit, while σ_{yy} , as well as σ_{zz} , shows a decay which can be described well by a dominant term B^{-2} . All the results agree with the high-field asymptotic behaviors listed Table 1. In addition, these conductivity elements under finite fields can be fitted to obtain global field dependences, as carried

out in Ref. 9.

In principle, there are two applications of the calculated band-resolved electric conductivity under the finite magnetic fields. With the determined relaxation time in each band, magnetoresistance study can be performed.¹⁰ Alternatively, combining the calculation results with the experimental measurements of conductance or resistance in different temperatures can lead to quantitative estimation about these scattering rates, including the impurity scattering and the electron-phonon coupling.⁹ It is worth pointing out that the efficient calculation provides reliable results and the simulation is performed at the accurate Fermi level. We suggest that this *ab initio* approach is helpful in the study of finite-field magnetic transport properties.

IV. LOW-FIELD HALL COEFFICIENT CALCULATION

Beyond the electric conductivity simulation under a finite magnetic field, we further applied the method in the low-field limit, where Hall effect is the major interest of the magnetic transport research. Previous studies^{14–16} followed the perturbation method, which adopts the power-series expansion of the magnetic field and gives the Hall coefficient for cubic crystals as

$$R_H = \sigma_H / \sigma_0^2. \quad (12)$$

Here σ_0 is the conductivity:

$$\sigma_0 = \frac{e^2}{3\hbar^2} \sum_{\mathbf{k}} \tau(\mathbf{k}) [\nabla_{\mathbf{k}} \varepsilon(\mathbf{k})]^2 \left[-\frac{\partial f(\varepsilon)}{\partial \varepsilon} \right], \quad (13)$$

and σ_H is the Hall conductivity:

$$\begin{aligned} \sigma_H = & \frac{e^3}{12} \sum_{\mathbf{k}} \tau^2(\mathbf{k}) \mathbf{v}(\mathbf{k}) [\text{Tr}(\mathbf{M}^{-1}) - \mathbf{M}^{-1}] \mathbf{v}(\mathbf{k}) \\ & \times \left[-\frac{\partial f(\varepsilon)}{\partial \varepsilon} \right]. \end{aligned} \quad (14)$$

\mathbf{M}^{-1} is the inverse mass tensor, and its elements are defined by

$$\mathbf{M}_{\alpha\beta}^{-1} = \frac{1}{\hbar^2} \frac{\partial^2 \varepsilon}{\partial k_{\alpha} \partial k_{\beta}}. \quad (15)$$

In this perturbation method, the evaluation of the second \mathbf{k} derivative of the band is a difficult task. It either gives unreliable results with the SKW interpolation in the presence of band crossings and/or near degeneracies,¹⁵ or follows a very complicated formula with the Wannier interpolation.¹⁶ For instance, Fig. 6 shows the complex band structure of fcc Pd. It has three energy bands across the Fermi energy, and multiple band crossings in the proximity of the Fermi level. Expensive computation is inevitable during the SKW interpolation due to the

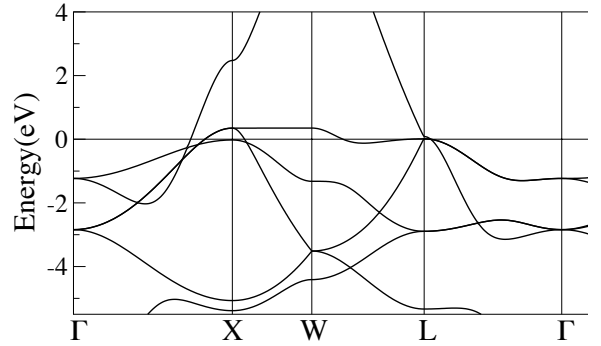


FIG. 6: The band structure of fcc Pd. The Fermi level is fixed at 0 eV.

complexity of the band structure, and the accuracy of the result will be threatened because of the band crossings. Even with the Wannier interpolation, the heavy computation of the inverse mass tensor still can not be avoided.

In our case, each element of the electric conductivity tensor can be obtained through Eq. (1). We can further evaluate the Hall resistivity according to the definition directly:³⁰

$$\rho_{yx} = \frac{-\sigma_{yx}}{\sigma_{xx}\sigma_{yy} - \sigma_{xy}\sigma_{yx}}. \quad (16)$$

Here we assume that the magnetic field is applied along the z -axis. The low-field limit is achieved with ρ_{yx} growing linearly with the field. The Hall coefficient is then given by the definition, as well:⁴

$$R_H = \frac{\rho_{yx}(B) - \rho_{xy}(-B)}{2B}. \quad (17)$$

This scheme is valid for metals with arbitrary structures. Particularly, in a crystal with threefold or fourfold symmetry about the magnetic field direction, rotation transformations require $\sigma_{xx} = \sigma_{yy}$ and $\sigma_{xy} = -\sigma_{yx}$. Thus we have

$$\rho_{yx} = \frac{\sigma_{xy}}{\sigma_{xx}^2 + \sigma_{xy}^2} \quad (18)$$

TABLE III: The calculated and experimentally observed Hall coefficient R_H , in the unit of $10^{-11} \text{m}^3/\text{C}$. Experimental data are all from Ref. 4.

	Li	Al	Cu	Pd	Mg
Ref. 14	-12.8	-1.7	-5.2	-6.0	-
Ref. 15	-12.4	-3.4	-4.9	-17	-
Ref. 16	-12.7	-2.5	-4.9	-11.9	-
This work	-13.0	-2.2	-5.2	-11.2	-10.4
Experiment	-15.5	-3.43	-5.17	-7.6	-8.3

to simplify the calculation in the application to all cubic and hexagonal systems. Throughout the calculation for the low-field Hall coefficient, we do not need to deal with the inverse mass tensor. The complexity of the band structure will not result in expensive computation.

We performed the calculation of the low-field Hall coefficient with Eqns. (16), (17), and (18) for typical cubic metals Li, Al, Cu, and Pd, as well as hcp Mg, where the magnetic field is along the hexagonal axis. The results are listed in Table 3. For Li, Al, and Cu, we find great agreement with previous simulations based on band structures fitted through TB scheme,¹⁴ *ab initio* calculation combined with SKW interpolation¹⁵ and Wannier interpolation.¹⁶ With a certain ratio between the relaxation times of the two bands of Al¹⁴, we can reproduce the experimental value in our simulation. In the case of Pd, the result with the SKW interpolation is not as satisfactory as those through TB and with the Wannier interpolation. It results from the complex band structure as analyzed above. Our result agrees excellently with that from Ref. 16, yet without the complicated evaluation of the inverse mass tensor. The discrepancy between calculated and experimental values was accounted for by the constant relaxation time approximation.^{14,34} For hcp Mg, our result is comparable to the experimental data with the magnetic field parallel to the hexagonal axis.

V. CONCLUSIONS

We have developed an efficient numerical scheme for the solution of the Boltzmann equation within the relaxation time approximation to obtain band-resolved electric conductivity under a finite magnetic field. It is based on the *ab initio* electronic structure calculation, and the

Wannier interpolation scheme is employed to analytically evaluate the velocities along the historical track of the electron wave packet. The simulation is guaranteed to be performed at the accurate FS by the modified self-adaptive Runge-Kutta method. As the first application, we have studied systematically the electric conductivity of normal-state MgB₂ with the magnetic field orientated parallel and normal to the *c*-axis, respectively. The multi-band characters within the individual bands are then revealed in detail.

During the conductivity calculation, the cyclotron motion of the wave packet driven by the magnetic field is simulated. We have taken advantage of these motions in the extremal orbits of MgB₂ to calculate the corresponding effective masses, with the results in good agreement with previous studies. It provides a direct simulation of the cyclotron motion and a reliable evaluation of the effective mass of the extremal orbit.

Another application of this method is the calculation of the low-field Hall coefficient as a universal approach for metals and semiconductors of arbitrary structures. We have reproduced the Hall coefficients for several typical cubic metals, and for hcp Mg as an example of non-cubic systems.

A remarkable appeal of this approach is that it provides an *ab initio* method to simulate the electric conductivity under a finite magnetic field. It is efficient and reliable owing to the Wannier interpolation scheme. Moreover, the direct simulation of the cyclotron motion is an elegant and useful application. The calculation of the low-field Hall coefficient is universal for crystals of arbitrary structures, and avoids all complicated computation of the second derivatives of the band. Therefore, this approach can be generally applied to a wide variety of systems for magnetic transport study.

ACKNOWLEDGEMENTS

We are grateful to Professor Junren Shi, Professor Haihu Wen and Dr. Huan Yang for helpful discussions of transport properties of MgB₂. This work is supported by the Natural Science Foundation of China (Nos.10674163, 10534030), the MOST Project (Nos. 2006CB921300, 2007CB925000), the Knowledge Innovation Project of Chinese Academy of Sciences.

* Electronic address: ygyao@aphy.iphy.ac.cn

¹ I. M. Lifshitz, M. Ia. Azbel, and M. I. Kaganov, J. Exptl. Theoret. Phys. (U. S. S. R.) **30**, 220 (1955) and **31**, 63 (1956) [translation: Soviet Phys. -JETP **3**, 143 (1956) and **4**, 41 (1957)].

² A. H. Wilson, *The Theory of Metals* (Cambridge University Press, Cambridge, UK, 1953).

³ J. M. Ziman, *Electrons and Phonons*, Classics Series (Oxford University Press, New York, 2001).

⁴ C. M. Hurd, *The Hall Effect in Metals and Alloys* (Plenum Press, New York, 1972).

⁵ C. W. J. Beenakker, Phys. Rev. Lett. **62**, 2020 (1989).

⁶ Chao Zhang and R. R. Gerhardts, Phys. Rev. B **41**, 12850 (1990).

- ⁷ Branko P. Stojković and David Pines, Phys. Rev. Lett. **76**, 811 (1996).
- ⁸ Rolf Menne and Rolf R. Gerhardts, Phys. Rev. B **57**, 1707 (1998).
- ⁹ Huan Yang, Yi Liu, Chenggang Zhuang, Junren Shi, Yugui Yao, Sandro Massidda, Marco Monni, Ying Jia, Xiaoxing Xi, Qi Li, Zi-Kui Liu, Qingrong Feng, and Hai-Hu Wen, Phys. Rev. Lett. **101**, 067001 (2008).
- ¹⁰ M. Monni, I. Pallecchi, C. Ferdegiani, V. Ferrando, A. Floris, E. Galleani D'Agliano, E. Lehmann, I. Sheikin, C. Tarantini, X. X. Xi, S. Massidda, and M. Putti, Europhys. Lett. **81**, 67006 (2008).
- ¹¹ D. D. Koelling and J. H. Wood, J. Comput. Phys., **67**, 253 (1986).
- ¹² Warren E. Pickett, Henry Krakauer and Philip B. Allen, Phys. Rev. B **38**, 2721 (1988).
- ¹³ H. Jones and C. Zener, Proc. Roy. Soc. (London) **A145**, 268 (1934).
- ¹⁴ Werner W. Schulz, Philip B. Allen, and Nandini Trivedi, Phys. Rev. B **45**, 10886 (1992).
- ¹⁵ Kentaro Uehara and John S. Tse, Phys. Rev. B **61**, 1639 (2000).
- ¹⁶ Jonathan R. Yates, Xinjie Wang, David Vanderbilt, and Ivo Souza, Phys. Rev. B **75**, 195121 (2007).
- ¹⁷ Nicola Marzari and David Vanderbilt, Phys. Rev. B **56**, 12847 (1997); Ivo Souza, Nicola Marzari, and David Vanderbilt, Phys. Rev. B **65**, 035109 (2001).
- ¹⁸ Peter E. Blöchl, O. Jepsen, and O. K. Andersen, Phys. Rev. B **49**, 16223 (1994).
- ¹⁹ Jun Nagamatsu, Norimasa Nakagawa, Takahiro Muranaka, Yuji Zenitani, and Jun Akimistu, Nature (London) **410**, 63 (2001).
- ²⁰ Xinjie Wang, Jonathan R. Yates, Ivo Souza, and David Vanderbilt, Phys. Rev. B **74**, 195118 (2006).
- ²¹ Neil W. Ashcroft and N. David Mermin, *Solid State Physics* (Harcourt, Orlando, 1976).
- ²² David Vanderbilt, Phys. Rev. B **41**, 7892 (1990).
- ²³ John P. Perdew, Kieron Burke, and Matthias Ernzerhof, Phys. Rev. Lett. **77**, 3865 (1996).
- ²⁴ A. B. Pippard, Rep. Progr. Phys. **23**, 176 (1960).
- ²⁵ E. Fawcett, Adv. Phys. **13**, 139 (1964).
- ²⁶ J. Kortus, I. I. Mazin, K. D. Belashchenko, V. P. Antropov, and L. L. Boyer, Phys. Rev. Lett. **86**, 4656 (2001).
- ²⁷ Amy Y. Liu, I. I. Mazin, and Jens Kortus, Phys. Rev. Lett. **87**, 087005 (2001)
- ²⁸ Yu Eltsev, K. Nakao, S. Lee, T. Masui, N. Chikumoto, S. Tajima, N. Koshizuka, and M. Murakami, Phys. Rev. B **66**, 180504(R) (2002)
- ²⁹ Qi Li, B. T. Liu, Y. F. Hu, J. Chen, H. Gao, L. Shan, H. H. Wen, A. V. Pogrebnyakov, J. M. Redwing, and X. X. Xi, Phys. Rev. Lett. **96**, 167003 (2006).
- ³⁰ A. B. Pippard, *Magnetoresistance in Metals* (Cambridge University Press, Cambridge, UK, 1989).
- ³¹ S. Elgazzar, P.M. Oppeneer, S.-L. Drechsler, R. Hayn, and H. Rosner, Solid State Commun. **121**, 99 (2002).
- ³² E. A. Yelland, J. R. Cooper, A. Carrington, N. E. Hussey, P. J. Meeson, S. Lee, A. Yamamoto, and S. Tajima, Phys. Rev. Lett **88**, 217002 (2002).
- ³³ I. I. Mazin and Jens Kortus, Phys. Rev. B **65**, 180510(R) (2002)
- ³⁴ T. Beaulac and P. B. Allen, J. Phys. F: Met. Phys. **13**, 383 (1982).